Numerical parametric lens for shifting, magnification, and complete aberration compensation in digital holographic microscopy

Tristan Colomb

Ecole Polytechnique Fédérale de Lausanne, Institute of Imaging and Applied Optics, CH-1015 Lausanne, Switzerland

Frédéric Montfort

Lyncée Tec SA, PSE-A, CH-1015 Lausanne, Switzerland

Jonas Kühn

Ecole Polytechnique Fédérale de Lausanne, Institute of Imaging and Applied Optics, CH-1015 Lausanne, Switzerland

Nicolas Aspert and Etienne Cuche

Lyncée Tec SA, PSE-A, CH-1015 Lausanne, Switzerland

Anca Marian and Florian Charrière

Ecole Polytechnique Fédérale de Lausanne, Institute of Imaging and Applied Optics, CH-1015 Lausanne, Switzerland

Sébastien Bourquin

Lyncée Tec SA, PSE-A, CH-1015 Lausanne, Switzerland

Pierre Marquet

Centre de Neurosciences Psychiatriques, Département de Psychiatrie DP-CHUV, Site de Cery, 1008 Prilly-Lausanne, Switzerland

Christian Depeursinge

Ecole Polytechnique Fédérale de Lausanne, Institute of Imaging and Applied Optics, CH-1015 Lausanne, Switzerland

Received March 20, 2006; revised June 21, 2006; accepted June 26, 2006; posted July 5, 2006 (Doc. ID 69126)

The concept of numerical parametric lenses (NPL) is introduced to achieve wavefront reconstruction in digital holography. It is shown that operations usually performed by optical components and described in ray geometrical optics, such as image shifting, magnification, and especially complete aberration compensation (phase aberrations and image distortion), can be mimicked by numerical computation of a NPL. Furthermore, we demonstrate that automatic one-dimensional or two-dimensional fitting procedures allow adjustment of the NPL parameters as expressed in terms of standard or Zernike polynomial coefficients. These coefficients can provide a quantitative evaluation of the aberrations generated by the specimen. Demonstration is given of the reconstruction of the topology of a microlens. © 2006 Optical Society of America

OCIS codes: 090.1760, 090.1000, 100.5070.

1. INTRODUCTION

Digital holographic microscopy (DHM) permits the reconstruction of the amplitude and the phase of an object wavefront from the acquisition of a single digital hologram. The principle consists of digitizing—with a CCD or other type of image sensor such as a complementary metal-oxide semiconductor (CMOS)—the interference between a reference and an object wave. Then, the wavefront is propagated from the hologram to the image plane within the Fresnel approximation by a numerical process. Two different numerical formulations are principally used: the single Fourier transform formulation (SFTF) or

 © 2006 Optical Society of America

the convolution formulation (CF) (for SFTF and CF, see Ref. 1). For both formulations, several parameters must be adjusted or calibrated[2–4] to achieve a correct reconstruction. Generally, the object wave contains aberrations including the tilt due to the off-axis geometry, the phase curvature introduced by the microscope objective (MO) used to increase the spatial resolution, and all the optical aberrations of the setup. It has previously been determined that the wavefront curvature introduced by the MO and lenses can be successfully removed,[3,5] as well as spherical aberration,[6] chromatic aberration,[7] astigmatism,[8,9] anamorphism,[10,11] and longitudinal image shifting introduced by a beam splitter cube.[12] Furthermore, a recent paper demonstrates that an automatic procedure for performing the adjustment of parameters associated with a standard polynomial model of aberrations allows one to achieve a complete compensation for phase aberrations in the image plane. This procedure can be applied without prior knowledge of physical parameters of the setup including, e.g., wave vector components, focal lengths, and positions of the optical components.[13]

On the other hand, the two reconstruction formulations SFTF and CF each have several advantages and disadvantages. In particular, within the framework of the SFTF, the scaling of the reconstructed region of interest (ROI) inside the reconstructed wave front is dependent on the reconstruction distance, the pixel number of the hologram, and the wavelength,[14] whereas the CF allows a scaling-free reconstruction of the ROI if there is no chromatic aberration in the setup. Consequently, different solutions have been proposed to control the scaling in SFTF to maintain the size of the ROI for a sequence of digital holograms recorded at different distances and to solve the problem of superimposition in multiwavelength methods for color holography,[15–18] tomographic holography,[19–25] or optical diffraction tomography.[26] Ferraro *et al.* proposed to control the scaling in SFTF by padding the holograms with zeros before the reconstruction.[14] This approach has the drawback of increasing the computational load because the number of hologram pixels is no longer a power of 2. Indeed, the standard fast Fourier transforms are optimized to compute the Fourier transform in time $O(N \log N)$ instead of $O(N^2)$ with $N=2^n$. Zhang *et al.* proposed another method to keep the original pixel number in SFTF.[27] A two-stage reconstruction algorithm controls the scale of the reconstructed image by placing between the hologram and the image planes a numerical lens with a focal length and a position defined by the chosen scale. The disadvantage of this method is the requirement of the computation of two propagations.

Finally, the curvature and the propagation direction of the object wave are sensitive to the wavelength used if the optics are not completely achromatic; thus a different scale and position of the ROI can also occur with CF.

We define in this paper a numerical parametric lens (NPL) placed in the hologram plane and/or in the image plane that achieves a complete compensation for aberrations (phase aberrations and image distortion) in SFTF or CF. The NPL shape is defined by standard or Zernike polynomial models whose parameters are adjusted automatically by a two-dimensional (2D) fitting procedure applied on specimen areas known to be flat instead of considering one-dimensional (1D) profiles as presented in Ref. 13. We demonstrate that the Zernike polynomial model of the NPL achieves quantitative measurements of specimen aberration properties. Then we demonstrate that placing the NPL in the hologram plane has several advantages. First, the correction of the tilt in the hologram plane allows an automatic centering of the ROI in the image plane that avoids any aliasing in CF or in SFTF with small reconstruction distance. Second, the complete aberration compensation in the hologram plane is preserved for any reconstruction distance.

We illustrate the technique by compensating for astigmatism produced by a cylindrical lens used as a MO and for high-order aberrations produced by a ball lens and a field lens introduced into the setup. Furthermore, chosen shift and magnification operations are demonstrated in CF by automatic computing of NPLs in hologram and image plans with the advantages of maintaining constant the original hologram pixel number and of using a unique numerical propagation.

2. EXPERIMENTAL SETUPS

Figure 1 presents the optical setups of transmission [Fig. 1(a)] and reflection [Fig. 1(b)] digital holographic microscopes. In both cases the basic architecture is that of a modified Mach–Zehnder interferometer. The light source depends on the targeted application: in Refs. 2 and 3 a He–Ne laser is used; low coherence sources[22] or a tunable source such as an optical parametric amplifier system[28] can be used.

In both configurations, a MO collects the object wave $\mathbf{O}$ transmitted or reflected by the specimen and produces a magnified image of the specimen at a distance d behind the CCD camera. As explained in detail in Ref. 3, this situation can be considered equivalent to a lensless holographic setup with an object wave $\mathbf{O}$ emerging directly from the magnified image of the specimen and not from the specimen itself.

In order to improve the sampling capacity of the CCD, a lens can be optionally introduced into the reference arm RL to produce in the CCD plane a spherical reference wave with a curvature very similar to the curvature created by the MO. At the exit of the interferometer, the interference between the object wave $\mathbf{O}$ and the reference wave $\mathbf{R}$ creates the hologram intensity

$$I_{\mathrm{H}}(x,y) = (\mathbf{R}+\mathbf{O})(\mathbf{R}+\mathbf{O})^* = |\mathbf{R}|^2 + |\mathbf{O}|^2 + \mathbf{R}^*\mathbf{O} + \mathbf{R}\mathbf{O}^*. \tag{1}$$

This hologram is digitized by a black and white CCD camera and then recorded on a computer. The digital hologram $I_{\mathrm{H}}(k,l)$ is an array of $N \times N$ (usually 512×512 or 1024×1024) 8-bit-encoded numbers resulting from the 2D sampling of $I_{\mathrm{H}}(x,y)$ by the CCD camera:

$$I_{\mathrm{H}}(k,l) = \int_{k\Delta x-\Delta x/2}^{k\Delta y+\Delta y/2} \int_{l\Delta y-\Delta y/2}^{l\Delta y+\Delta y/2} I_{\mathrm{H}}(x,y)\,\mathrm{d}x\,\mathrm{d}y, \tag{2}$$

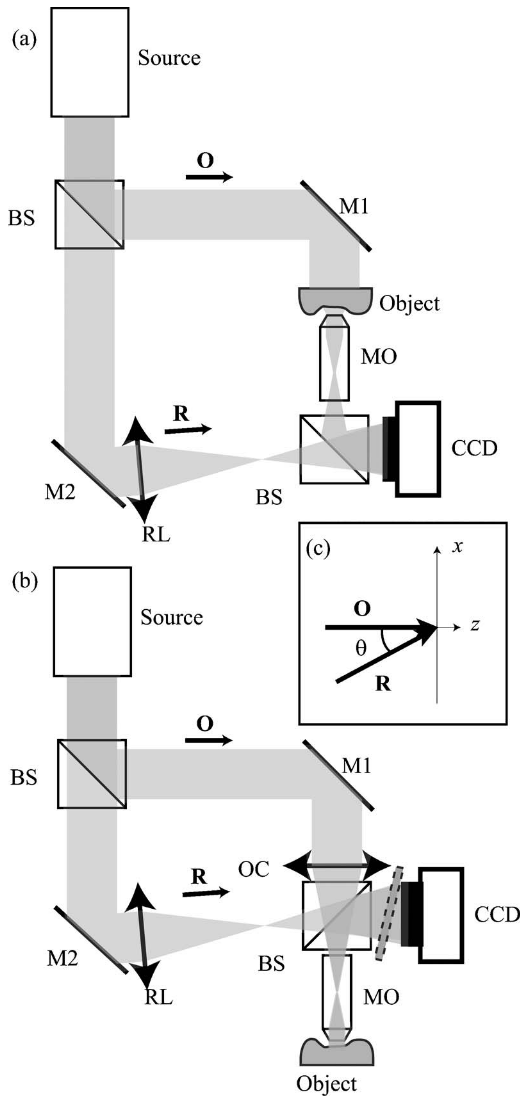

Fig. 1. Digital holographic microscope, (a) transmission and (b) reflection setups. **O** object wave; **R** reference wave; BS beam splitter; M1, M2 mirrors; MO microscope objective, RL lens in the reference wave, OC condenser in the object wave. For demonstration purposes a tilted plate is introduced between the BS and the CCD to intentionally produce aberrations. (c) Detail of the off-axis geometry.

where k,l are integers, and Δx, Δy define the sampling intervals in the hologram plane (pixel size). The different terms of this hologram are the zeroth order of diffraction ($|\mathbf{R}|^2+|\mathbf{O}|^2$), the real image ($\mathbf{R}\mathbf{O}^*$), and the virtual image ($\mathbf{R}^*\mathbf{O}$). This hologram can be numerically filtered as shown in Ref. 29 to produce a hologram containing only the virtual image term

$$I_{\mathrm{H}}^{\mathrm{F}} = \mathbf{R}^*\mathbf{O}. \tag{3}$$

We now introduce the NPL into the reconstruction process. NPLs mimic pure phase objects and are defined as two arrays of unit-amplitude complex numbers Γ^{H} and Γ^{I} placed respectively in the hologram (H) and image (I) planes. The numerically reconstructed wavefronts Ψ are also computed in the SFTF or CF as follows:

$$\Psi_{\mathrm{SFTF}}(m,n) = \Gamma^{\mathrm{I}}(m,n)A \exp\left[\frac{i\pi}{\lambda d}(m^2\Delta\xi^2 + n^2\Delta\eta^2)\right] \times \mathrm{FFT}\left\{\Gamma^{\mathrm{H}}(k,l)I_{\mathrm{H}}^{\mathrm{F}}(k,l) \times \exp\left[\frac{i\pi}{\lambda d}(k^2\Delta x^2 + l^2\Delta y^2)\right]\right\}, \tag{4}$$

$$\Psi_{\mathrm{CF}}(m,n) = \Gamma^{\mathrm{I}}(m,n)A \times \mathrm{FFT}^{-1}\{\mathrm{FFT}[\Gamma^{\mathrm{H}}(k,l)I_{\mathrm{H}}^{\mathrm{F}}(k,l)] \times \exp[-i\pi\lambda d(\nu_k^2 + \nu_l^2)]\}, \tag{5}$$

where FFT is the fast Fourier transform; m, n, k, l are integers ($-N/2 < m,n,k,l \leq N/2$); d is the reconstruction distance; $A = \exp(i2\pi d/\lambda)/(i\lambda d)$; λ is the wavelength; $\nu_k = k/(N\Delta x)$, $\nu_l = l/(N\Delta y)$ are the spatial frequency coordinates; and $\Delta\xi$ and $\Delta\eta$ are the sampling intervals in the image plane defined as

$$\Delta\xi = \Delta\eta = \frac{\lambda d}{N\Delta x}. \tag{6}$$

In SFTF, a scaling factor results between the hologram size and the reconstructed ROI defined by the scale factors α and given by

$$\alpha_\xi = \frac{\Delta x}{\Delta\xi} = \frac{N\Delta x^2}{\lambda d}, \quad \alpha_\eta = \frac{\Delta y}{\Delta\eta} = \frac{N\Delta y^2}{\lambda d}. \tag{7}$$

We should remark that the particular case of $\Gamma^{\mathrm{H}} = \mathbf{R}$ and $\Gamma^{\mathrm{I}} = 1$ corresponds to the standard numerical expression of the Fresnel propagation.[2]

Let us define a NPL as an array of unit amplitude complex numbers that can be defined by standard or Zernike polynomials:

$$\Gamma_{\mathrm{S}}(m,n) = \exp\left(-i\frac{2\pi}{\lambda}\sum_{\alpha=\beta=0}^{\alpha+\beta=o} P_{\alpha\beta} m^\alpha m^\beta\right), \tag{8}$$

$$\Gamma_{\mathrm{Z}}(m,n) = \exp\left(-i\frac{2\pi}{\lambda}\sum_{\alpha=0}^{o} P_\alpha Z_\alpha\right), \tag{9}$$

where $P_{\alpha\beta}$ and P_α are the NPL parameters and o is the polynomial order. The Zernike polynomials, further designated by Z_α, are defined in Table 1 following the ZEMAX classification.[30] We recall that the Zernike polynomials are defined in a unit circle.

Now we represent the parametric numerical lenses in the planes $\mathrm{P} = \mathrm{H}, \mathrm{I}$ as the multiplication of three different lenses used to shift (Sh), magnify (M), and compensate (C) for aberrations with the polynomial model $\mathrm{PM} = \mathrm{S}, \mathrm{Z}$:

$$\Gamma^{\mathrm{P}} = \Gamma_{\mathrm{S}}^{\mathrm{P,Sh}} \Gamma_{\mathrm{S}}^{\mathrm{P,M}} \Gamma_{\mathrm{PM}}^{\mathrm{P,C}}. \tag{10}$$

The numerical multiplication of these complex arrays is achieved pixel-by-pixel and is therefore commutative. However, the procedure to define them is not. The application order of the NPL is first to compensate for the aberrations, then to do numerical magnification, and finally to apply the numerical shift. But to simplify the explanation, we present the different methods in the reverse order.

Table 1. Zernike Standard Coefficients in ZEMAX Classification

Polynomial	Cartesian Form	Description
Z_0	1	Piston
Z_1	$\sqrt{4}x$	Tilt x
Z_2	$\sqrt{4}y$	Tilt y
Z_3	$\sqrt{3}(2x^2+2y^2-1)$	Power
Z_4	$\sqrt{6}(2xy)$	Astig y
Z_5	$\sqrt{6}(x^2-y^2)$	Astig x
Z_6	$\sqrt{8}(3x^2y+3y^3-2y)$	Coma y
Z_7	$\sqrt{8}(3x^3+3xy^2-2x)$	Coma x
Z_8	$\sqrt{8}(3x^2y-y^3)$	Trefoil y
Z_9	$\sqrt{8}(x^3-3xy^2)$	Trefoil x
Z_{10}	$\sqrt{5}(6x^4+12x^2y^2+6y^4 -6x^2-6y^2+1)$	Primary Spherical
Z_{11}	$\sqrt{10}(4x^4-3x^2+3y^2-4y^4)$	2ary Astig x
Z_{12}	$\sqrt{10}(8x^3y+8xy^3-6xy)$	2ary Astig y
Z_{13}	$\sqrt{10}(x^4-6x^2y^2+y^4)$	Tetrafoil x
Z_{14}	$\sqrt{10}(4x^3y-4xy^3)$	Tetrafoil y
Z_{15}	$\sqrt{12}(10x^5+20x^3y^2+10xy^4 -12x^3-12xy^2+3x)$	2ary Coma x
Z_{16}	$\sqrt{12}(10x^4y+20x^2y^3+10y^5 -12x^2y-12y^3+3y)$	2ary Coma y
Z_{17}	$\sqrt{12}(5x^5-10x^3y^2-15xy^4 -4x^3+12xy^2)$	2ary Trefoil x
Z_{18}	$\sqrt{12}(15x^4y+10x^2y^3 -5y^5-12x^2y+4y^3)$	2ary Trefoil y
Z_{19}	$\sqrt{12}(x^5-10x^3y^2+5xy^4)$	Pentafoil x
Z_{20}	$\sqrt{12}(5x^4y-10x^2y^3+y^5)$	Pentafoil y
Z_{21}	$\sqrt{7}(20x^6+60x^4y^2+60x^2y^4 +20y^6-30x^4-60x^2y^2 -30y^4+12x^2+12y^2-1)$	2ary Spherical
Z_{22}	$\sqrt{14}(30x^5y+60x^3y^3+30xy^5 -40x^3y-40xy^3+12xy)$	3ary Astig y
Z_{23}	$\sqrt{14}(15x^6+15x^4y^2-20x^4 +6x^2-15x^2y^4-15y^6 +20y^4-6y^2)$	3ary Astig x

3. PRINCIPLE OF AUTOMATIC PROCEDURES

In Ref. 13, a simple procedure has already been presented that is performed in the image plane and permits adjustment of the standard polynomial parameters $P_{\alpha\beta}$ by a 1D least-squares fitting procedure applied to profiles extracted from areas of the specimen known to be flat. Drawbacks of the 1D procedure are that the method is limited to a standard polynomial model and requires the use of a reference hologram (without specimen) to compute the cross terms of the standard polynomial (as $x^{\alpha}y^{\beta}$, $\alpha,\beta\neq 0$). We present here a more general and efficient 2D fitting procedure applied on specimen areas known to be flat. The fitting procedure is illustrated in the image plane of a United States Air Force (USAF) test target hologram recorded with a reflection setup [see Fig. 1(b)] where a tilted thick plate is introduced between the beam splitter BS and the CCD camera in order to produce aberrations.

In the assumed flat specimen area F defined by the mosaic of white rectangle on the surface [see Fig. 2(a)] N_{pts} points (γ_m,ζ_n) are selected $[(\gamma_m,\zeta_n)\in \mathrm{F}]$. The N_{pts} measured phase values are converted to optical path lengths (OPL) $Y(\gamma_m,\zeta_n)$ that satisfy the N_{pts} following equations depending on the model used [Eqs. (8) and (9)]:

$$Y(\gamma_m,\zeta_n)=\sum_{\alpha=\beta=0}^{\alpha+\beta=o} a_{\alpha\beta}S_{\alpha\beta}, \quad S_{\alpha\beta}=\gamma_m^{\alpha}\zeta_n^{\beta}, \tag{11}$$

$$Y(\gamma_m,\zeta_n)=\sum_{\alpha=0}^{\alpha=o} a_{\alpha}Z_{\alpha}, \tag{12}$$

where γ_m and ζ_n are computed from the pixel position (m,n) to satisfy the condition that F is inscribed in the unit circle and o is the polynomial order. Equations (12) and (11) define two linear systems with N_{pts} equations and, respectively, a number of unknown coefficients $o+1$ and $(o^2+3o+2)/2$ (for example, for a second order of the standard polynomial the six unknown coefficients are a_{00}, a_{10}, a_{01}, a_{20}, a_{02}, and a_{11}). Because a great number of points can be selected in an image the system is always

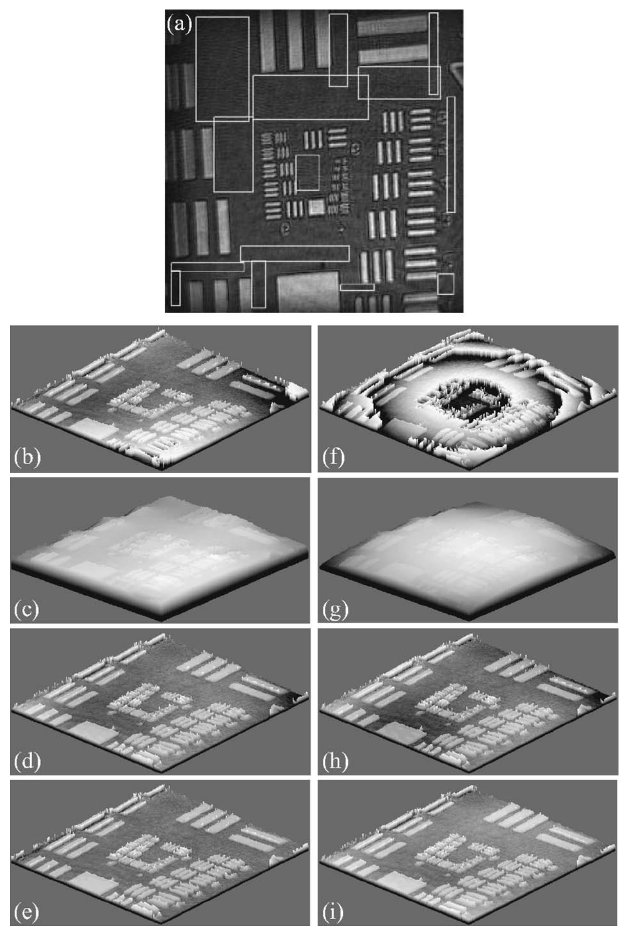

Fig. 2. Two-dimensional fitting procedure with standard polynomial model (left column) and Zernike polynomial model (right), (a) the reconstructed amplitude contrast with the assumed flat areas F situated inside the white rectangles. (b) and (f) reconstruction with initial parameters computed with 1D procedure. (c) and (g) 2D unwrap of (b) and (f), respectively (d) and (e) respectively, the corrections with six and ten adjusted standard polynomial coefficients $(o=2,3)$. (h) and (i) respectively, the correction with six and eight adjusted Zernike polynomial coefficients $(o=5,7)$.

overdetermined. For example assuming 3% flat area in a 256×256 image, 1966 equations can be defined, for example, to compute 28 unknown factors for $o=6$ in the standard polynomial model. These systems are solved by computing in the least-squares sense the solution of

$$\mathbf{M}\times\mathbf{A}_{\mathrm{M}}=\mathbf{Y}, \tag{13}$$

where $\mathbf{M}=\mathbf{S}$, $\mathbf{Z}$ is the matrix of fitting polynomials in the standard or Zernike model, $\mathbf{Y}$ is the vector of the OPL measured values $Y(\gamma_m,\zeta_n)$, and $\mathbf{A}_{\mathrm{M}}$ is the vector of the unknown coefficients $a_{\alpha\beta}$ or a_{α}.

As already developed in Ref. 13, an iterative procedure can be used to adjust the parameter vector $\mathbf{P}_{\mathrm{M}}$:

$$\mathbf{P}_{\mathrm{M}}^{(i)}=\mathbf{P}_{\mathrm{M}}^{(i-1)}+\mathbf{A}_{\mathrm{M}}^{(i)}. \tag{14}$$

The NPLs for aberration compensation are therefore given by

$$\Gamma_{\mathrm{M}}^{\mathrm{P,C}}=\exp\left[-i\frac{2\pi}{\lambda}\mathbf{P}_{\mathrm{M}}\cdot\mathbf{M}\right]. \tag{15}$$

Obviously, this iterative procedure fails if there are phase jumps in the areas F due to initial NPLs parameters being too different from the optimal ones. Therefore a simple first-step procedure consists of computing initial parameters $\mathbf{P}_{\mathrm{M}}^{(0)}$ with a 1D fitting method[13]:

$$\mathbf{P}_{\mathrm{S}}^{(0)}=\begin{bmatrix}0 & P_{10}^{1D} & P_{01}^{1D} & P_{20}^{1D} & P_{02}^{1D}\end{bmatrix}, \tag{16}$$

$$\mathbf{P}_{\mathrm{Z}}^{(0)}=\begin{bmatrix}0 & \dfrac{P_{10}^{1D}}{2} & \dfrac{P_{01}^{1D}}{2}\end{bmatrix}, \tag{17}$$

where $P_{\alpha\beta}^{1D}$ are the parameters adjusted by the 1D fitting procedure [see Figs. 2(b) and 2(f)].

The second step consists of performing a 2D unwrap on the resulting reconstructed phase in order to suppress possible remaining phase jumps due to aberrations [see Figs. 2(c) and 2(g)].

Finally, the 2D fitting procedure is applied by increasing the polynomial order when necessary. Figures 2(d), 2(e), 2(h), and 2(i) present the reconstructed phase obtained with the NPL adjustment in, respectively, the standard and Zernike polynomial models. The polynomial order used for Figs. 2(d) and 2(e) are, respectively, $o=2$ (six parameters) and $o=3$ (ten parameters), and those used for Figs. 2(h) and 2(i) are, respectively, $o=5$ (six parameters) and $o=7$ (eight parameters).

4. RESULTS

A. Application to Quantitative Aberration Measurement

As already established in Ref. 13, the automatic adjustment of NPL in the image plane can be used to compensate for the specimen curvature. Here, we demonstrate that the Zernike polynomial model not only allows us to compensate for the curvature of the specimen but also measures quantitatively the aberrations in term of Zernike coefficients. Figure 3 presents different representations of the same microlens recorded in a transmission setup. The first step consists of compensating for the setup aberration by applying the 2D fitting procedure in the Zernike model on areas around the microlens where

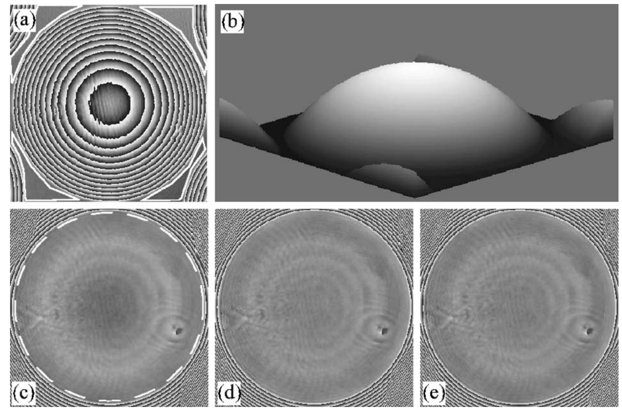

Fig. 3. (a) Microlens phase by applying 2D fitting procedure with Zernike polynomial on points included in areas indicated by white lines. (b) Perspective representation of 2D phase unwrap of (a). (c)–(e) Microlens shape compensation with Zernike formulation with (c) 10 parameters, (d) 11 parameters, (e) 21 parameters.

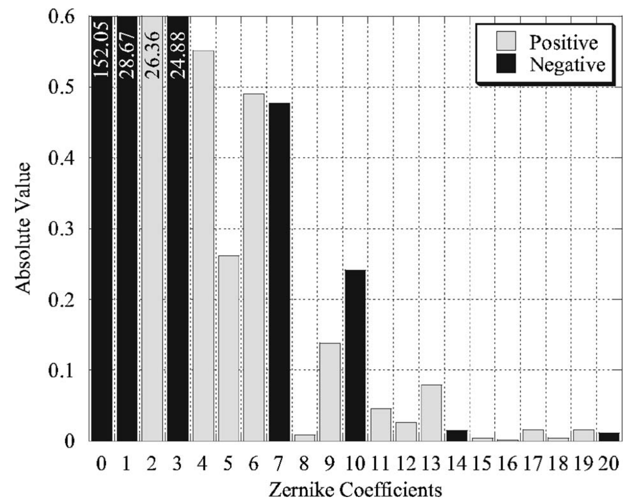

Fig. 4. Repartition of Zernike coefficients for an adjustment of 21 coefficients. The absolute coefficient values are plotted. Black and gray patterns indicate, respectively, negative and positive values.

the surface is known to be flat [areas shown by white lines in Fig. 3(a)]. The resulting image allows a perspective representation of the curvature induced by the microlens in Fig. 3(b) by applying a 2D phase unwrap on the image in Fig. 3(a). Now, the 2D fitting procedure applied in the area of the microlens [dashed white circle in Fig. 3(c)] allows us to compensate for the specimen curvature. Figure 3(c) corresponds to the adjustment of Zernike coefficients up to Z_9. The result of the adjustment of the next Zernike coefficient Z_{10} is shown in Fig. 3(d). The "flattening" operation performs better and reveals that this microlens generates important spherical aberrations (see Table 1). Finally, Fig. 3(e) shows that the increase of the polynomial order up to Z_{20} does not provide a better aberration compensation.

Figure 4 summarizes the repartition of the aberrations of the microlens. It shows an important astigmatism (Z_4 and Z_5; more in direction y than x), a coma amplitude (Z_6 and Z_7) equivalent in the two directions, a trefoil (Z_8 and Z_9) negligible in direction y, and finally an important primary spherical aberration (Z_{10}). In addition the representation of the "flattened" microlens and the coefficient parameters provides a wealth of data on the microlens such as surface topography, radius of curvature, lens height, and surface roughness.[31]

B. Automatic Region of Interest Centering

As a result of the off-axis geometry of the holographic setups, the carrier frequencies of the real or virtual images are not in the center of the spectrum as presented in Fig. 5(a). This results in a spatial separation of the different diffraction orders during the reconstruction process.[32] In our setups (Fig. 1), the object and reference waves propagate, respectively, collinearly and with an angle θ from the normal vector to the hologram plane during the recording process [Fig. 6(a)]. Let us consider now the wavefront reconstruction from a filtered hologram containing only a virtual image in two different ways.

The first way [Fig. 6(b)] corresponds to the reconstruction process with the digital reference wave outside the Fresnel integral, as described in Ref. 13. In this case, the reconstructed wavefront in the hologram plane is $\mathbf{R}^{*}\mathbf{O}$ and propagates at an angle $-\theta$. The ROI is therefore shifted in the image plane [see Fig. 7(a) with SFTF and Fig. 7(e) with CF].

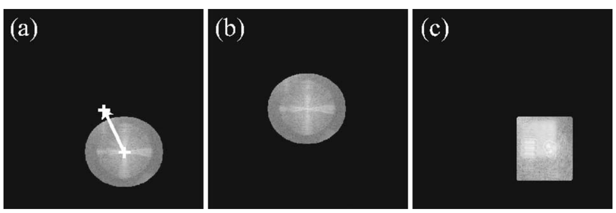

Fig. 5. Procedure of spectrum centering. (a) Initial filtered spectrum, (b) spectrum centered. The arrow represents the shift between the amplitude maximum of the frequencies associated with the virtual image and the center of the entire spectrum. (c) Spectrum of a hologram for which the curvatures of the reference and object waves are different, inducing a nonpunctual central frequency in the spectrum.

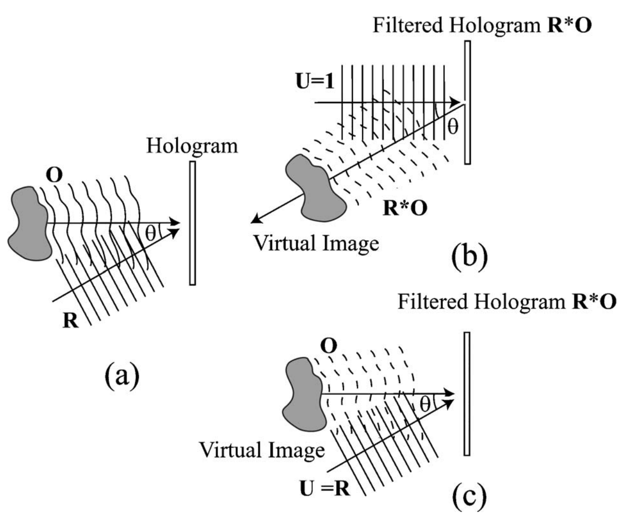

Fig. 6. Principle of digital reconstruction process to center the ROI. (a) Hologram recording, (b) reconstruction with a digital reference wave $\mathbf{U}=1$ (the ROI is not centered), (c) reconstruction with a digital reference wave $\mathbf{U}=\mathbf{R}$ (the ROI is centered).

The second way [Fig. 6(c)] corresponds to the optical reconstruction process with the reference wave $\mathbf{R}$ as illuminating wave. Digitally this amounts to the same thing as computing Eq. (4) or (5) with $\Gamma^{H,C}=\mathbf{R}$. In this case, the wavefront in the hologram plane is $\mathbf{O}$, which propagates normally to the hologram plane. Therefore, the ROI is centered in the reconstructed wavefront.

The shift of the ROI in the first reconstruction method is not convenient in CF because aliasing appears as presented in Figs. 7(e) and 7(f). In the case of SFTF, it may not be a problem if the scale factors defined in Eq. (7) are sufficiently small to avoid any aliasing [Figs. 7(a) and 7(b)]. But because these scale factors are inversely proportional to the reconstruction distance d, aliasing could nevertheless appear when d becomes too small (Fig. 8). Therefore for any formulation, it is more judicious to suppress the shift or the ROI as presented in Figs. 7(g) and 7(h) for CF and in Fig. 8(d) for SFTF with small reconstruction distance.

The procedure to shift the ROI to the center can be achieved with two methods. The first one, called spectrum centering, consists of shifting the carrier frequency of the virtual (real) image to the center of the filtered hologram spectrum, applying an inverse Fourier transform of the resulting spectrum, and then propagating the wavefront. A simpler procedure consists of detecting the position of the amplitude maximum corresponding to the carrier frequency of the virtual image [see Fig. 5(a)]. This position is then shifted to the center of the spectrum [see Fig. 5(b)]. This method has two main drawbacks. The first is that the shifting amplitude is limited by the pixel accuracy. The second concerns the central frequency spreading [see Fig. 5(c)] that results from a difference of curvature between the reference and object waves and makes the virtual image carrier frequency impossible to center by a simple maximum-amplitude detection.

We propose to compute automatically the tilt parameters $P_{10}^{H,C}$ and $P_{01}^{H,C}$ of $\Gamma_{S}^{H,C}$ by selecting profiles or areas known to be flat in the hologram plane and then proceeding with the fitting procedure. Because the image in the hologram plane is defocused flat areas would seem to be difficult to define. In fact, the contributions of the phase diffraction pattern are averaged and are therefore negligible if the selected profiles or areas are sufficiently far from the specimen. Figure 9 presents the hologram plane phase image before [Fig. 9(a)] and after [Fig. 9(c)] the tilt adjustment and their corresponding image plane amplitude [Figs. 9(b) and 9(d)] reconstructed in SFTF. In this example, the 1D procedure is applied to the selected black profiles of Fig. 9(a). The resulting phase curvature in Fig. 9(c) corresponds to the noncorrected curvature induced by the MO. The ROI is centered in the image plane [Fig. 9(d)] and we have $\Gamma^{H,C}=\mathbf{R}$.

C. Manual Shifting in Convolution Formulation

It may be interesting to shift the ROI manually in a specific region, for example, in order to compensate for a specimen translation between two hologram acquisitions. For this purpose, we show how to define the shifting NPLs $\Gamma^{H,Sh}$ and $\Gamma^{I,Sh}$ in the CF. The procedure has three principal steps. First, the operator draws two points defining the desired shift (arrows in Fig. 10). The second

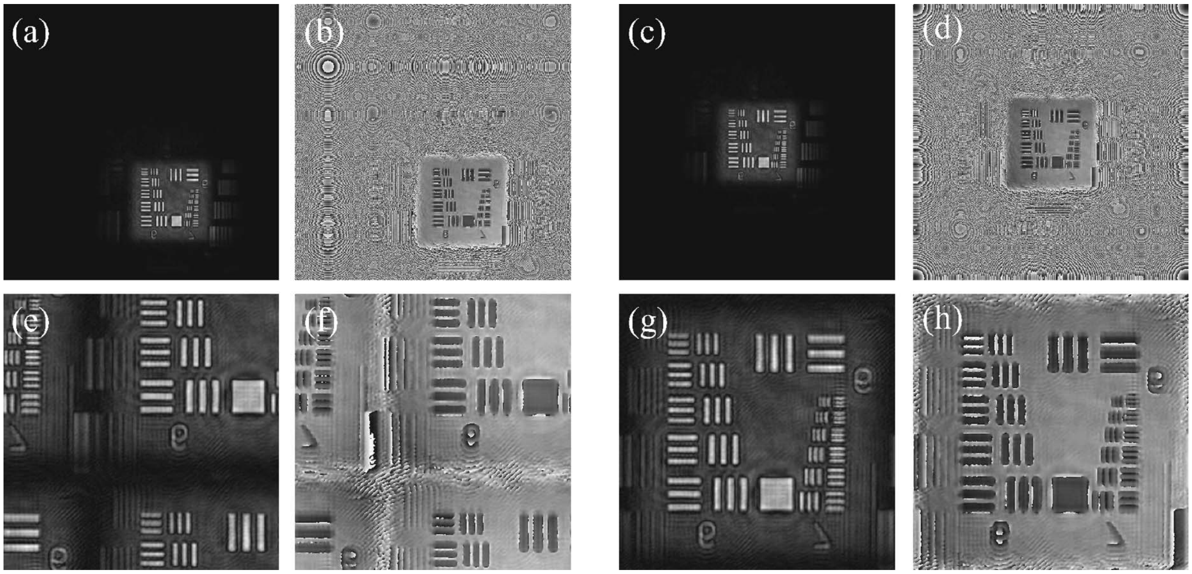

Fig. 7. Comparison between SFTF [(a)–(d)] and CF [(e)–(h)], with [(c), (d), (g), (h)] or without [(a), (b), (e), (f)] ROI centering. (a), (c), (e), (g) are amplitude images and (b), (d), (f), (h) the corresponding phase reconstructions.

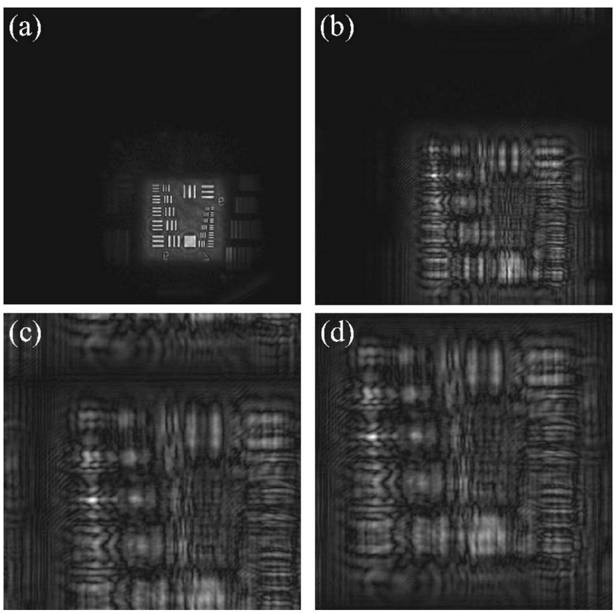

Fig. 8. Aliasing appears when the reconstruction distance is too small. (a) $d=11\,\text{cm}$, (b) $d=5\,\text{cm}$, (c) aliasing at $d=3.3\,\text{cm}$. With ROI centering, the reconstruction (d) can be achieved without aliasing.

step consists of computing the parameters $P_{10}^{\mathrm{H,Sh}}$ and $P_{01}^{\mathrm{H,Sh}}$ of $\Gamma^{\mathrm{H,Sh}}$. These parameters can be easily computed by considering Fig. 11. Let us define the chosen shift in the two directions by

$$\Delta S_j = N_{\mathrm{S}j}\Delta j, \tag{18}$$

where $j=x,y$ and $N_{\mathrm{S}j}$ is the number of pixels to shift in the j direction. The shifting NPL is written as

$$\Gamma_{\mathrm{S}}^{\mathrm{H,Sh}}(\mathbf{x}) = \exp\left[i\frac{2\pi}{\lambda}\hat{\mathbf{S}}\mathbf{x}\right] = \exp\left[i\frac{2\pi}{\lambda}(S_x m\Delta x + S_y n\Delta y)\right], \tag{19}$$

where $\hat{\mathbf{S}}$ is the unit shift vector. The components of the vector $\hat{\mathbf{S}}$ are

$$S_j = \sin(\theta_j) = \sin\left[\arctan\left(\frac{\Delta S_j}{d}\right)\right]. \tag{20}$$

The parameters $P_{10}^{\mathrm{H,Sh}}$ and $P_{01}^{\mathrm{H,Sh}}$ are also

$$P_{10}^{\mathrm{H,Sh}} = -\sin\left[\arctan\left(\frac{\Delta S_x}{d}\right)\right]\Delta x,$$

$$P_{01}^{\mathrm{H,Sh}} = -\sin\left[\arctan\left(\frac{\Delta S_y}{d}\right)\right]\Delta y. \tag{21}$$

Obviously this shift introduced into the hologram plane produces a tilt in the image plane that should be compensated for. We introduce therefore a predicted compensating shifting NPL in the image plane defined as

$$\Gamma_{\mathrm{S}}^{\mathrm{I,Sh}}(m,n) = \exp\left[-i\frac{2\pi}{\lambda}(P_{10}^{\mathrm{I,Sh}}m + P_{01}^{\mathrm{I,Sh}}n)\right], \tag{22}$$

where $P_{10}^{\mathrm{I,Sh}}=-P_{10}^{\mathrm{H,Sh}}$ and $P_{01}^{\mathrm{I,Sh}}=-P_{01}^{\mathrm{H,Sh}}$. Figures 10(c) and 10(d) show the shifted amplitude and phase reconstructions.

It is important to note that this shifting method is limited by the chosen shift and by the reconstruction distance. Indeed, the Nyquist sampling criterion requires that the highest spatial frequency introduced by the shift should be less than the cutoff frequency $1/(2\Delta x)$. In other words, it means that the shifting angle θ may not exceed the maximum value $\theta_{\max}$ given by

$$\theta \le \theta_{\max} = \arcsin\left(\frac{\lambda}{2\Delta x}\right). \tag{23}$$

The shifting is also limited by Eq. (23), which gives the inequality

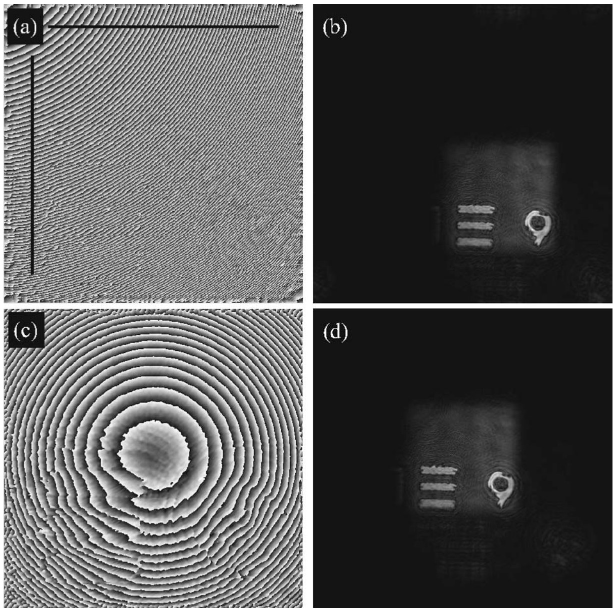

Fig. 9. Adjustment of the tilt parameters of the NPL Γ^{H} by applying 1D procedure along black profiles. (a) The initial phase in the hologram plane, (b) the corresponding amplitude reconstruction in SFTF, (c) tilt-corrected phase in the hologram plane, (d) the corresponding centered amplitude reconstruction.

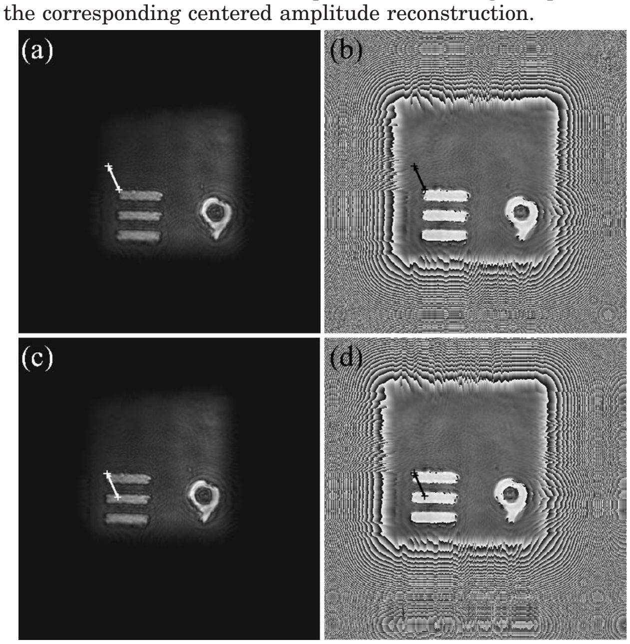

Fig. 10. Shifting procedure: (a) and (b) show, respectively, the amplitude and phase reconstructions after tilt compensation. The arrows define the chosen translation of the ROI. (c) and (d) show the respective amplitude and phase shifted reconstructions.

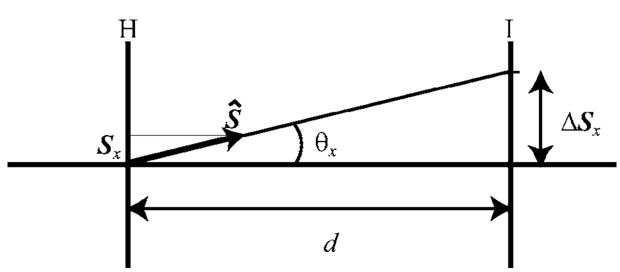

Fig. 11. H, hologram plane; I, image plane; ΔS_x, chosen shift in the direction x; d, reconstruction distance; θ_x, shifting angle.

$$\arctan\left(\frac{\Delta Sj}{d}\right) \leq \theta_{\max} = \arcsin\left(\frac{\lambda}{2\Delta x}\right). \qquad (24)$$

For example, with a sampling $\Delta x = 6.7\ \mu\text{m}$, a wavelength $\lambda = 633\ \text{nm}$, and a reconstruction distance $d = 1\ \text{cm}$, the maximum number of pixels to shift is $N_{\text{Smax}} = d/\Delta x \tan[\arcsin(\lambda/2\Delta x)] = 70.58$ pixels. This limitation is not a problem, because the chosen shift is usually limited to a maximum of a few dozen pixels and the reconstruction distance is also usually ≈ 5 cm, which corresponds to $N_{\text{Smax}} = 352$ pixels.

The automatic and manual shift methods are very efficient in comparing or superposing different wavefront reconstructions that appear usually in different areas of the image plane. In particular, these methods are very useful in polarization imaging with DHM[33] in which two fringe patterns are recorded on the same hologram. For this application, two different orthogonal, polarization-state reference waves with two different propagation directions are used in order to separate spatially the two reconstructed virtual images. The automatic and manual shifts constitute a very simple way to perform a subpixel superposition of the two wavefronts so as to compute the polarization parameters.

D. Numerical Magnification in Convolution Formulation

We propose here to adjust the magnification of the ROI by computing the parametric focal length of the NPL characterized by $\Gamma^{H,M}$ and $\Gamma^{I,M}$. This method keeps constant the pixel number of the hologram and is based on a single propagation. Let us define the hologram plane H where the NPL with focal distance f is placed, the original image plane I defined by the reconstruction distance d (position of the reconstructed virtual image), and the final image plane I′ defined by the reconstruction distance d'. By these definitions, the real object (having the same size as the virtual image) is at a distance d from the hologram plane. The magnification M is also calculated from the real object and image distances:

$$M = -d'/(-d) = d'/d. \qquad (25)$$

The lens equation gives

$$1/f = 1/(-d) + 1/d'. \qquad (26)$$

Let us define now the magnification NPL described by a thin lens transmittance[32] or from Eq. (8):

$$\Gamma^{H,M}(m,n) = \exp\left[i\frac{2\pi}{\lambda}\frac{1}{2f}(m^2\Delta x^2 + n^2\Delta y^2)\right], \qquad (27)$$

$$\Gamma^{H,M}(m,n) = \exp\left[-i\frac{2\pi}{\lambda}(P_{20}^{H,M}m^2 + P_{02}^{H,M}n^2)\right], \qquad (28)$$

where $P_{20}^{H,M} = P_{02}^{H,M}$ are the magnification parameters associated with the focal length of the lens:

$$P_{20}^{H,M} = P_{02}^{H,M} = \frac{\Delta x^2}{2f}. \qquad (29)$$

Finally, with Eqs. (25), (26), and (29), the new reconstruction distance and the parameter $P_{02}^{H,M}$ can be computed from M and the initial reconstruction distance d:

$$d' = Md, \tag{30}$$

$$P_{02}^{\mathrm{H,M}} = P_{20}^{\mathrm{H,M}} = \left(\frac{1}{M} - 1\right)\frac{\Delta x^2}{2d}. \tag{31}$$

Obviously, as for the shifting method, the phase curvature introduced in the hologram plane by the NPL has to be compensated for in the new image plane I′. The predicted compensation for the magnification NPL in the image plane is

$$\Gamma^{\mathrm{I,M}}(m,n) = \exp\left[i\frac{2\pi}{\lambda}\frac{1}{2(f-d')}(m^2\Delta x^2 + n^2\Delta y^2)\right], \tag{32}$$

$$\Gamma^{\mathrm{I,M}}(m,n) = \exp\left[-i\frac{2\pi}{\lambda}(P_{20}^{\mathrm{I,M}}m^2 + P_{02}^{\mathrm{I,M}}n^2)\right], \tag{33}$$

where the parameters are

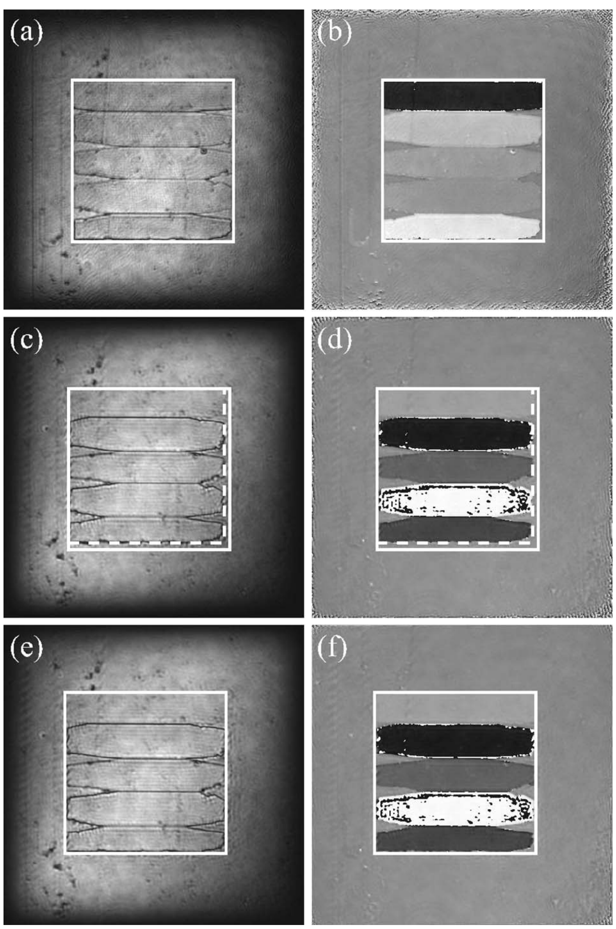

Fig. 12. Amplitude and phase reconstructions are presented, respectively, on the left and on the right. The reconstructions are done from a hologram recorded with (a), (b) $\lambda_1 = 480$ nm; (c)–(f) $\lambda_2 = 700$ nm. The white rectangle defines the reference size. The white dashed rectangle defines the size of the same object without performing magnification. Images in (e), (f) are reconstructed from the same hologram as in (b), (c) after performing a magnification procedure $M = 1.0038$ defined by the ratio of the rectangle sizes.

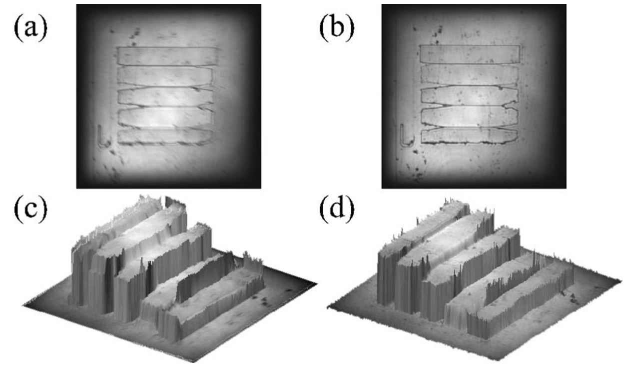

Fig. 13. (a), (b) Mean amplitude reconstructed from 20 holograms recorded with different wavelengths and (c), (d) mapping of it on the 3D topography of the specimen. Images in (b), (d) are processed with shift and magnification compensation.

$$P_{20}^{\mathrm{I,M}} = P_{02}^{\mathrm{I,M}} = \frac{\Delta x^2(M-1)}{2M^2 d}. \tag{34}$$

An example of application of this method is presented in Fig. 12. Two different holograms of the same object have been recorded with two different wavelengths $\lambda_1 = 480$ nm [Figs. 12(a) and 12(b)] and $\lambda_2 = 700$ nm [Figs. 12(c)–12(f)]. We note that the size of the observed object is different because of the nonachromatic MO used in the setup (difference between the dashed and solid white rectangles). The ratio of the rectangle sizes defines a magnification $M = 1.0038$. The magnification procedure allows us to achieve the scaled reconstruction presented in Figs. 12(e) and 12(f).

We can mention here that a different scaling in the two directions can be done by applying two different magnifications in the corresponding directions.

The shifting and magnification procedure can be applied in the context of submicrometer optical tomography by multiple wavelength DHM. The principle consists of recording several holograms at different wavelengths (typically 20 holograms with wavelengths between 480 nm and 700 nm) with a reflection digital holographic microscope. The reconstruction of these holograms and their processing allows tomographic imaging.[34] An important point for the tomographic reconstruction process is that the size of the ROI on each reconstructed image should be identical. Because of the presence of chromatic aberration and/or laser pointing changes for each wavelength, the reconstruction distance, the size, and the position of the ROI change as shown in Figs. 12(a)–12(d). Figure 13 compares the mean amplitude computed from the 20 holograms [Figs. 13(a) and 13(b)] and the mapping of it on the 3D topography of the specimen [Figs. 13(c) and 13(d)] when the magnification and the shift are either applied to all 20 superimposed, reconstructed images [Figs. 13(b) and 13(d)] or not applied [Figs. 13(a) and 13(c)]. We can see clearly that the image in Fig. 13(a) is blurred whereas that in Fig. 13(b) is not. The improvement of the method is also visible in Fig. 13(d) where the noise on the specimen edges is clearly diminished.

E. Complete Aberration Compensation

Let us assume that the specimen does not introduce aberrations but only a phase delay $\varphi(x,y)$. In the known flat areas this term $\varphi(x,y)=c$ (c a constant) for any plane, neglecting the diffraction pattern due to the specimen in defocused planes. The reference and object waves can be defined more generally by introducing the respective phase aberration terms $W_{\mathbf{R}}$ and $W_{\mathbf{O}}$:

$$\mathbf{R}(x,y) = |\mathbf{R}|\exp[i(k_x x + k_y y)]\exp[iW_{\mathbf{R}}(x,y)], \tag{35}$$

$$\mathbf{O}(x,y) = |\mathbf{O}|\exp[i\varphi(x,y)]\exp[iW_{\mathbf{O}}(x,y)]. \tag{36}$$

These phase aberration terms can be astigmatism, defocus aberration, spherical aberration, and so on. Here, we assume that the amplitude is not affected by the aberrations. The filtered hologram of Eq. (3) becomes

$$I_{\mathrm{H}}^{\mathrm{F}} = |\mathbf{R}||\mathbf{O}|\exp[-i(k_x x + k_y y)]\exp[i(\varphi + W_{\mathbf{O}} - W_{\mathbf{R}})]. \tag{37}$$

The method of suppressing the aberration term $W=W_{\mathbf{O}} - W_{\mathbf{R}}$ consists simply of applying the 1D or the 2D fitting procedure on the filtered hologram phase. The adjustment of the standard or Zernike polynomial parameters of Γ^{H} is achieved by considering the known flat areas in the hologram plane.

We have already shown that the tilt adjustment in this plane permits us to place the ROI in the center of the image plane [see Figs. 14(a)–14(c)]. By increasing the order, it is possible to "flatten" the phase in the hologram plane as presented in Fig. 14(d). Because of the compensation for the curvature of the object wave, the NPL works also as a magnification lens: The reconstruction distances with or without NPL are different, consistent with the equations presented in Subsection 4.D.

In Fig. 14 the initial reconstruction distance is $d = 17.46$ cm [Figs. 14(b) and 14(c)], the adjusted term $P_{02}^{\mathrm{H}} = 1.24558 \times 10^{-10}$ provides a magnification $M=0.5122$, and a new reconstruction distance $d=8.78$ cm is used to reconstruct Figs. 14(e) and 14(f). Because the reconstruction was achieved in SFTF, no magnification of the ROI appears. It is important to note that no NPL is applied in the image plane for the reconstruction of the images in Figs. 14(c) and 14(f). We see that the correction in the hologram plane avoids the utilization of the NPL in the image plane for any reconstruction distance. Indeed, the term $\Gamma^{\mathrm{H}} I_{\mathrm{H}}^{\mathrm{F}}$ is similar to a plane wave modulated by the phase delay induced by the specimen. The propagation of this plane wave therefore conserves a constant phase value in the areas known to be flat, and the phase aberrations are also corrected for any reconstruction distance.

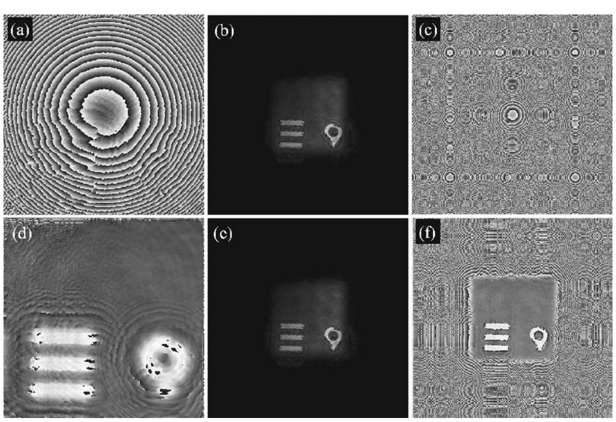

Fig. 14. (a) Correction of the tilt in the hologram plane and respective (b) amplitude and (c) phase reconstructions in SFTF at a distance $d=17.46$ cm without NPL in image plane. (d) High-order correction in the hologram plane and respective (e) amplitude and (f) phase reconstruction at a distance $d=8.78$ cm. The correction in the hologram plane is preserved along the direction of propagation and a numerical lens is no longer necessary in the image plane.

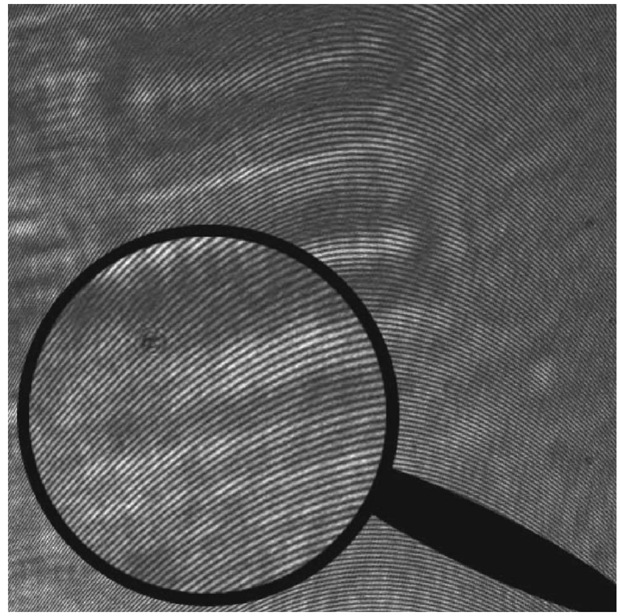

Fig. 15. Hologram of USAF test target recorded with a cylindrical lens as MO.

5. APPLICATIONS AND DISCUSSION

A. Compensation for Astigmatism Induced by a Cylindrical Lens

Grilli *et al.* present theoretically the potentialities of DHM for astigmatism evaluation and compensation.[9] Furthermore, De Nicola *et al.* present a method with two different reconstruction distances to achieve astigmatism compensation.[10] Here we demonstrate experimentally that astigmatism introduced by a cylindrical lens can be compensated for by a NPL in the hologram plane only. This cylindrical lens is introduced in a reflection setup in the place of the MO [see Fig. 1(b)]. Figure 15 presents the hologram of a USAF test target recorded with this setup. The fringe pattern is unusual and corresponds to the interference between an ellipsoidal wave and a plane wave.

Figure 16 presents the amplitude reconstruction with SFTF along the z direction for different reconstruction distances. Because of astigmatism of the cylindrical lens, there are two partial focal points, one for each direction, localized at $d=\infty$ and $d=5.5$ cm (the amplitude reconstruction shows a vertical line). The image is almost focused at $d=23.3$ cm as also shown on Fig. 17(b). This astigmatism can be revealed better by using CF. Because aliasing appears in CF [Fig. 17(a)] because of a larger magnification of the cylindrical lens in the horizontal direction, a numerical magnification $M=0.3$ is applied; the results can

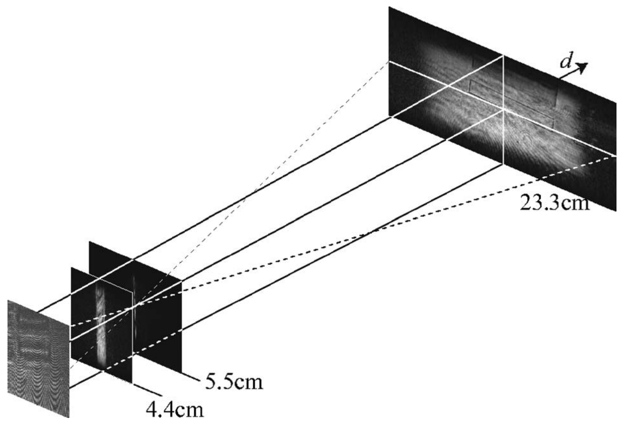

Fig. 16. Amplitude reconstruction for different distances of reconstruction. Because of the astigmatism of the cylindrical lens, there are two different focal points located at $d=5.5$ cm and $d=\infty$. The reconstructed image is focused at $d=23.3$ cm.

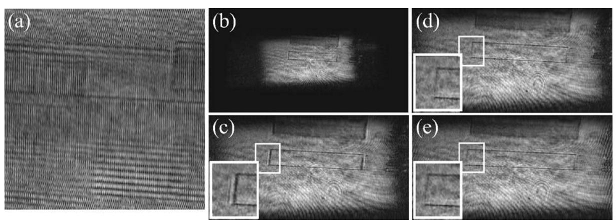

Fig. 17. Amplitude reconstruction with different parameters, (a) CF, $M=1$, $d=23.3$ cm; (b) SFTF, $d=23.3$ cm, (c) CF, $M=0.3$, $d=6.99$. The astigmatism shown in detail in (c) is compensated by (d) the adjustment of $P_{20}^{\mathrm{H,A}}=0.11\times10^{-10}$ or by (e) defining two reconstruction distances $d_1=6.99$ cm and $d_2=7.92$ cm.

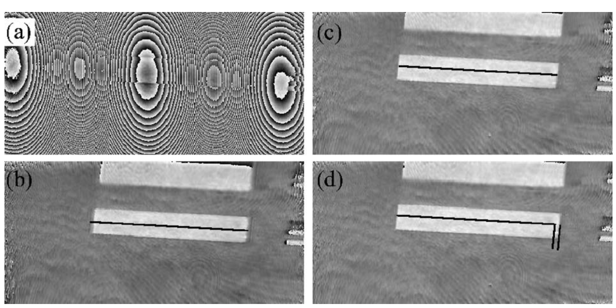

Fig. 18. (a) Phase reconstruction with $P_{20}^{\mathrm{H,A}}=0.11\times10^{-10}$ without $\Gamma^{\mathrm{I,C}}$; the other images are compensated with $\Gamma^{\mathrm{I,C}}$, (b) $P_{20}^{\mathrm{H,A}}=0$, (c) $P_{20}^{\mathrm{H,A}}=0.11\times10^{-10}$, and (d) two reconstruction distances. The black lines have the same length and reveal a dilatation in the image in the horizontal direction for (d).

be observed in Fig. 17(c). The inset in Fig. 17(c) shows clearly that the vertical edges of the USAF step are not focused.

Let us define a new NPL written $\Gamma^{\mathrm{H,A}}$ that is dedicated to astigmatism compensation and defined by two second-order standard polynomial coefficients $P_{02}^{\mathrm{H,A}}$ and $P_{20}^{\mathrm{H,A}}$. Figures 17(d) and 17(e) present, respectively, the compensation for this astigmatism by the manual adjustment of $P_{20}^{\mathrm{H,A}}=0.11\times10^{-10}(P_{02}^{\mathrm{H,A}}=0)$ and by the adjustment of two reconstruction distances $d_1=6.99$ cm and $d_2=7.92$ cm as explained in Ref. 10. We can see in the insets that the two methods correct the astigmatism very well, but there is a very small difference between the ROI sizes: The image in Fig. 17(e) is larger in the horizontal direction.

Figure 18 reveals that the two astigmatism compensations used for the amplitude image are not sufficient to compensate for the other phase aberrations if no NPL is applied in the image plane [see Fig. 18(a)]. Therefore, the NPL $\Gamma^{\mathrm{I,C}}$ is adjusted in the image plane for the different cases of astigmatism correction: Fig. 18(b) without correction, Fig. 18(c) with $P_{20}^{\mathrm{H,C}}=0.11\times10^{-10}$, and Fig. 18(d) with two reconstruction distances. One should note that the NPL method preserves the geometry [the step length is equal between Figs. 18(b) and 18(c)], whereas this is not the case for the two-reconstruction-distance technique of Fig. 18(d).

Finally, we compare the two astigmatism compensation methods when the 2D fitting procedure is applied in the hologram plane to adjust $\Gamma_{\mathrm{S}}^{\mathrm{H,C}}$. It is also important to remark that, as established for the magnification method, the introduction of $\Gamma^{\mathrm{H,A}}$ when $\Gamma^{\mathrm{H,C}}$ has already been adjusted introduces a phase curvature in the image plane that can be compensated with the predicted NPL $\Gamma^{\mathrm{I,A}}$ in the image plane with $P_{20}^{\mathrm{I,A}}$ or $P_{02}^{\mathrm{I,A}}$ computed from Eqs. (31) and (33):

$$P_{20}^{\mathrm{I,A}}=\frac{\Delta x^2}{(\Delta x^2/2P_{20}^{\mathrm{H}})-d}. \tag{38}$$

Figure 19 presents the phase image in the hologram plane before [Fig. 19(a)] and after [Fig. 19(b)] the 2D fitting procedure for $\Gamma_{\mathrm{S}}^{\mathrm{H,C}}$. The "flattening" operation in the hologram plane increases the astigmatism as presented in Figs. 20(a) and 20(b). Indeed, two very different reconstruction distances allow focus along the horizontal [Fig. 20(a), $d=13.3$ cm] or vertical direction [Fig. 20(b), $d=-6.9$ cm]. The astigmatism is therefore compensated by the two-reconstruction-distance method [Fig. 20(c)] or by the adjustment of $\Gamma^{\mathrm{H,A}}$ for the cases of two reconstruction distances: Fig. 20(d) corresponds to $d=-7.1$ cm, $P_{02}^{\mathrm{H,A}}=-4.7\times10^{-10}$ and Fig. 20(e) to $d=7.95$ cm, $P_{20}^{\mathrm{H,A}}=4.7\times10^{-10}$.

In short, we show that the two astigmatism compensation methods are not equivalent in terms of geometry conservation. Indeed, the two-reconstruction-distance method deforms the reconstructed images, whereas this is not the case with our method. Furthermore, our method involving aberration compensation in the hologram plane achieves astigmatism compensation for the amplitude and phase images for any reconstruction distances. These

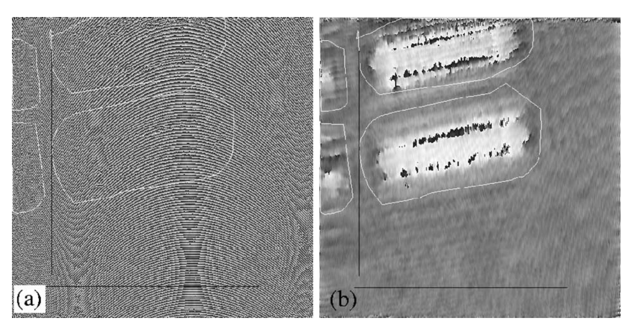

Fig. 19. Phase image in hologram plane: (a) without $\Gamma_{\mathrm{S}}^{\mathrm{H,C}}$ adjustment, (b) after adjustment of standard polynomial order $o=3$. The straight black lines define the profiles used to set the initial values of 2D fitting parameters, and the curved white lines delimit the areas excluded from the areas known to be flat.

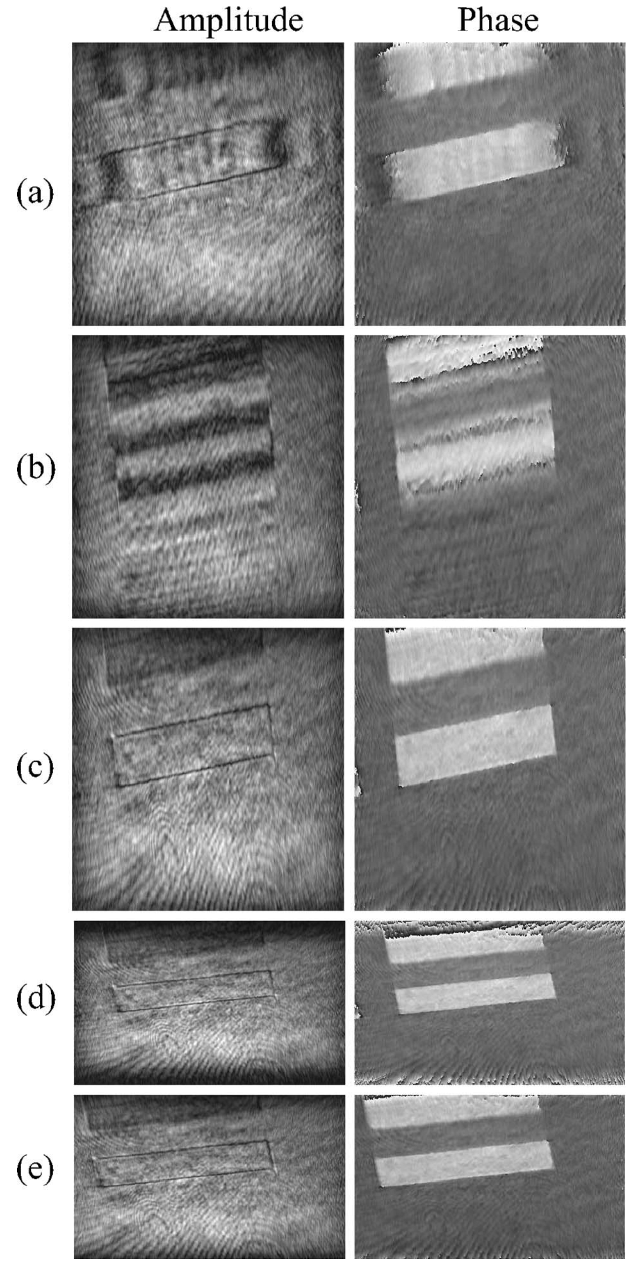

Fig. 20. Amplitude (left) and phase (right) reconstructions after $\Gamma_S^{H,C}$ adjustment: (a) $d=13.3$ cm, (b) $d=-6.9$ cm, (c) $d_1=13.3$ cm and $d_2=-6.9$ cm, (d) $M=0.56$ ($d=-7.1$ cm) and $P_{02}^{H}=-4.7\times10^{-10}$, (e) $M=0.56$ ($d=7.95$ cm) and $P_{20}^{H}=4.7\times10^{-10}$.

results show that a cylindrical lens can be used advantageously instead of a MO to study specimens with different characteristic length and width such as optical fibers or waveguides.

B. Ball Lens as Microscope Objective

To illustrate further the different techniques of aberration compensation, we introduce a ball lens (Edmund ball lens SF8 of 2 mm diameter, $n=1.689$) as MO and a field lens between the BS and the CCD camera in a transmission setup [Fig. 1(a)]. The positions of the ball lens, the field lens, and the CCD are adjusted to produce very strong aberrations. A liquid of index $n=1.6$ is used as immersion fluid. The specimen is a USAF test target. Figure 21 presents the comparison between different methods of aberration compensation. In the first column, only the tilt is compensated for in the hologram plane. It is evident that aberrations are introduced by the ball lens that deforms the USAF test target [Figs. 21(b) and 21(c)]. Furthermore, the NPL applied in the image plane does not succeed in correctly "flattening" the phase image. In the second column, a seventh-order standard polynomial 2D fitting is applied to the hologram. The correction of distortion is good, and the phase aberrations are well compensated.

The residual distortion comes from the nonexact assumption of a nonaberrated amplitude of the reference and object waves. Indeed, some part of the phase aberrations introduced by the ball lens and/or the field lens is converted to amplitude aberrations by the optical propagation of the wave in the path of the ball lens, the field lens, and the CCD camera. Because the NPL compensates only for phase aberrations in the hologram plane, the residual amplitude aberrations in the hologram plane are not compensated for by the automatic adjustment. This residual amplitude aberration in the hologram plane is converted to distortion in the image plane as shown in Figs. 22(b) and 22(c).

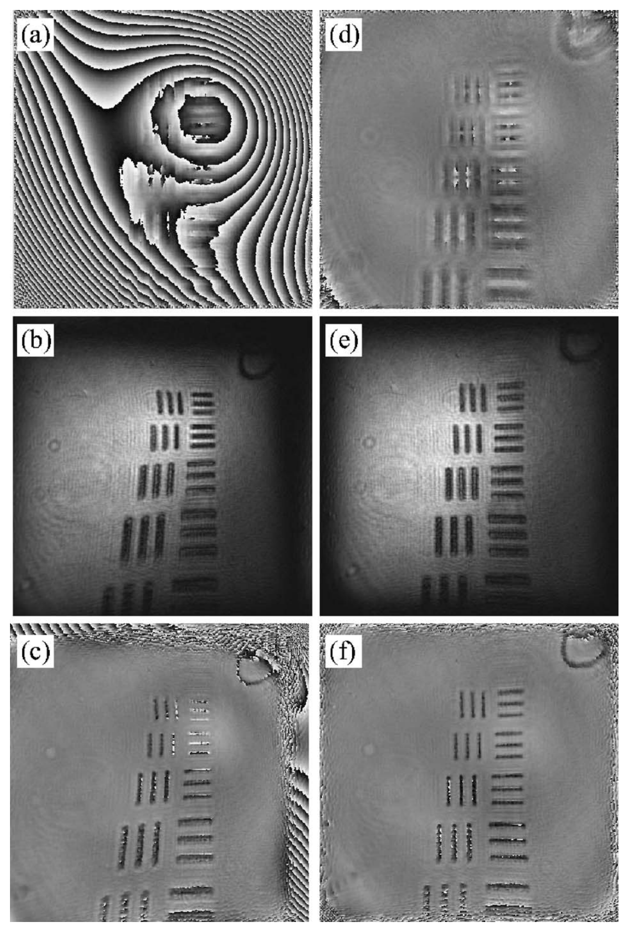

Fig. 21. (a)–(c) The correction of the tilt is done in the hologram plane, and the aberration compensation is performed in the image plane. (d),(e) Compensation with $\Gamma_S^{H,C}$ with seventh-order standard polynomial 2D fitting. (a), (d) Hologram, plane phase images. (b), (e) and (c), (f), respectively, amplitude and phase images in the image plane. The image distortion clearly visible in (b), (c) is compensated in (e), (f).

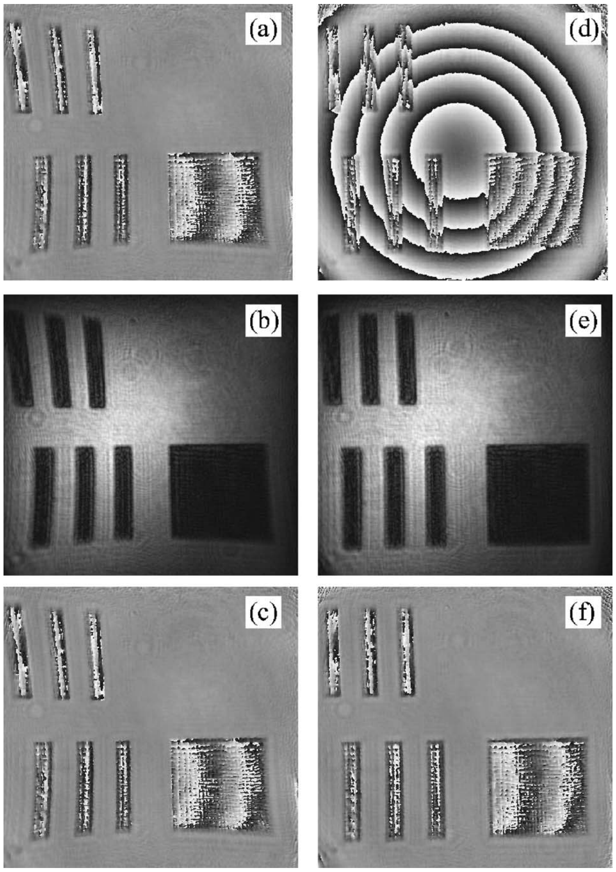

Fig. 22. (a)–(c) Compensation with $\Gamma_S^{H,C}$ with eighth-order standard polynomial 2D fitting; (d)–(f) after adding manual adjustment of primary spherical Zernike term $Z_{10}=9.83\times10^{-7}$ and a compensation of the resulting phase deformation in the image plane by an automatic adjustment of $\Gamma_S^{I,C}$ (six orders). (a) and (d) show the hologram plane phase image; (b), (e) and (c), (f), respectively, show the amplitude and phase images in the image plane. The image distortion clearly visible in (b), (c) is totally compensated in (e), (f).

To overcome this residual distortion, a NPL could be placed in the plane where the aberrations are introduced, or in other words in the plane where there are phase-only aberrations. We do not treat this solution further for two reasons. First, it is not evident that such a plane exists, because the aberrations are produced by different optics (here principally by the ball lens and the field lens, but the other optics do contribute also). Second, even if this plane existed and its position could be defined, two numerical propagations would need to be performed to reconstruct the corrected wavefront (from the hologram plane to the phase-only aberration plane and then from the phase-only aberration plane to the image plane), and that would not be suitable in terms of time-consuming reconstruction.

To keep to a single numerical propagation, the distortion compensation is applied in the hologram plane by adjusting manually the NPL parameters to minimize the distortion in the image plane. In Fig. 22(d), the primary spherical term parameter of the NPL $\Gamma_Z^{H,C}$ is adjusted ($Z_{10}=9.83\times10^{-7}$) to compensate for the distortion [see Figs. 22(e) and 22(f)] that is not yet totally compensated for by the 2D fitting procedure method [see Figs. 22(b) and 22(c)]. We note that the introduced phase term in the hologram plane [see Fig. 22(d)] produces a phase deformation in the image plane that is compensated automatically by a sixth-order NPL $\Gamma_S^{I,C}$ as presented in the phase image [see Fig. 22(f)].

6. CONCLUSION

We have presented in this paper numerical methods to compensate for all aberrations. Classically, aberrations are minimized by use of different well-designed optical components placed successively in the optical path. Our technique is similar but has the advantage of using a maximum of two numerical parametric lenses placed in the hologram and in the image plane. Furthermore, we demonstrated that these numerical lenses can be computed to achieve a numerical magnification and shift of the region of interest. This last feature gives us the ability to compensate for chromatic aberrations, the scaling coming from different reconstruction distances, and the specimen shift that can occur between two hologram acquisitions.

In addition, the technique has the advantage of minimizing the number of parameters that should be adjusted by the operator. Indeed, automatic fitting procedures showed that phase aberrations and image distortion can be suppressed, in particular with the compensation for aberration introduced by the use of a cylindrical lens or a ball lens as MO. This feature allows low-cost setups that could be constructed with inexpensive optical components that produce aberrations.

ACKNOWLEDGMENTS

The authors thank M. Gu and H. Tiziani for fruitful discussion and acknowledge gratefully research grant 205320-103885/1 from the Swiss National Science Foundation and research grant 7152.1 from the Innovation Promotion Agency (KTI/CTI).

Corresponding author T. Colomb's e-mail address is tristan.colomb@a3.epfl.ch.

REFERENCES

1. U. Schnars and W. P. O. Jüptner, "Digital recording and numerical reconstruction of holograms," Meas. Sci. Technol. **13**, R85–R101 (2002).
2. E. Cuche, F. Bevilacqua, and C. Depeursinge, "Digital holography for quantitative phase-contrast imaging," Opt. Lett. **24**, 291–293 (1999).
3. E. Cuche, P. Marquet, and C. Depeursinge, "Simultaneous amplitude-contrast and quantitative phase-contrast microscopy by numerical reconstruction of Fresnel off-axis holograms," Appl. Opt. **38**, 6994–7001 (1999).
4. P. Ferraro, S. De Nicola, A. Finizio, G. Coppola, S. Grilli, C. Magro, and G. Pierattini, "Compensation of the inherent wave front curvature in digital holographic coherent microscopy for quantitative phase-contrast imaging," Appl. Opt. **42**, 1938–1946 (2003).
5. G. Pedrini, S. Schedin, and H. J. Tiziani, "Aberration compensation in digital holographic reconstruction of microscopic objects," J. Mod. Opt. **48**, 1035–1041 (2001).
6. A. Stadelmaier and J. H. Massig, "Compensation of lens aberrations in digital holography," Opt. Lett. **25**, 1630–1632 (2000).
7. S. De Nicola, A. Finizio, G. Pierattini, D. Alfieri, S. Grilli, L.

Sansone, and P. Ferraro, "Recovering correct phase information in multiwavelength digital holographic microscopy by compensation for chromatic aberrations," Opt. Lett. **30**, 2706–2708 (2005).

8. S. De Nicola, P. Ferraro, A. Finizio, and G. Pierattini, "Wave front reconstruction of Fresnel off-axis holograms with compensation of aberrations by means of phase-shifting digital holography," Opt. Lasers Eng. **37**, 331–340 (2002).
9. S. Grilli, P. Ferraro, S. De Nicola, A. Finizio, G. Pierattini, and R. Meucci, "Whole optical wavefields reconstruction by digital holography," Opt. Express **9**, 294–302 (2001).
10. S. De Nicola, P. Ferraro, A. Finizio, and G. Pierattini, "Correct-image reconstruction in the presence of severe anamorphism by means of digital holography," Opt. Lett. **26** 974–976 (2001).
11. S. De Nicola, A. Finizio, G. Pierattini, P. Ferraro, and D. Alfieri, "Angular spectrum method with correction of anamorphism for numerical reconstruction of digital holograms on tilted planes," Opt. Express **13**, 9935–9940 (2005).
12. S. De Nicola, P. Ferraro, A. Finizio, S. Grilli, and G. Pierattini, "Experimental demonstration of the longitudinal image shift in digital holography," Opt. Eng. (Bellingham) **42**, 1625–1630 (2003).
13. T. Colomb, E. Cuche, F. Charrière, J. Kühn, N. Aspert, F. Montfort, P. Marquet, and C. Depeursinge, "Automatic procedure for aberration compensation in digital holographic microscopy and applications to specimen shape compensation," Appl. Opt. **45**, 851–863 (2006).
14. P. Ferraro, S. De Nicola, G. Coppola, A. Finizio, D. Alfieri, and G. Pierattini, "Controlling image size as a function of distance and wavelength in Fresnel-transform reconstruction of digital holograms," Opt. Lett. **29**, 854–856 (2004).
15. J. Kato, I. Yamaguchi, and T. Matsumura, "Multicolor digital holography with an achromatic phase shifter," Opt. Lett. **27**, 1403–1405 (2002).
16. I. Yamaguchi, T. Matsumura, and J. Kato, "Phase-shifting color digital holography," Opt. Lett. **27**, 1108–1110 (2002).
17. P. Almoro, M. Cadatal, W. Garcia, and C. Saloma, "Pulsed full-color digital holography with a hydrogen Raman shifter," Appl. Opt. **43**, 2267–2271 (2004).
18. B. Javidi, P. Ferraro, S.-H Hong, S. D. Nicola, A. Finizio, D. Alfieri, and G. Pierattini, "Three-dimensional image fusion by use of multiwavelength digital holography," Opt. Lett. **30**, 144–146 (2005).
19. G. Indebetouw and P. Klysubun, "Optical sectioning with low coherence spatiotemporal holography," Opt. Commun. **172**, 25–29 (1999).
20. M. K. Kim, "Tomographic three-dimensional imaging of a biological specimen using wavelength-scanning digital interference holography," Opt. Express **7**, 305–310 (2000).
21. A. Dakoff, J. Gass, and M. K. Kim, "Microscopic three-dimensional imaging by digital interference holography," J. Electron. Imaging **12**, 643–647 (2003).
22. P. Massatsch, F. Charrière, E. Cuche, P. Marquet, and C. Depeursinge, "Time-domain optical coherence tomography with digital holographic microscopy," Appl. Opt. **44**, 1806–1812 (2005).
23. A. Thelen, J. Bongartz, D. Giel, S. Frey, and P. Hering, "Iterative focus detection in hologram tomography," J. Opt. Soc. Am. A **22**, 1176–1180 (2005).
24. L. Martínez-León, G. Pedrini, and W. Osten, "Applications of short-coherence digital holography in microscopy," Appl. Opt. **44**, 3977–3984 (2005).
25. L. Yu and M. K. Kim, "Wavelength scanning digital interference holography for variable tomographic scanning," Opt. Express **13**, 5621–5627 (2005).
26. F. Charrière, A. Marian, F. Montfort, J. Kühn, T. Colomb, E. Cuche, P. Marquet, and C. Depeursinge, "Cell refractive index tomography by digital holographic microscopy," Opt. Lett. **31**, 178–180 (2006).
27. F. C. Zhang, I. Yamaguchi, and L. P. Yaroslavsky, "Algorithm for reconstruction of digital holograms with adjustable magnification," Opt. Lett. **29**, 1668–1670 (2004).
28. F. Montfort, "Tomography using multiple wavelengths in digital holographic microscopy," Ph.D. dissertation (Ecole Polytechnique Fédérale de Lausanne, Lausanne, 2005).
29. E. Cuche, P. Marquet, and C. Depeursinge, "Spatial filtering for zero-order and twin-image elimination in digital off-axis holography," Appl. Opt. **39**, 4070–4075 (2000).
30. "ZEMAX: Optical Design Program, User's Guide, Version 10.0" (Focus Software, Tucson, 2001), pp. 126–127.
31. F. Charrière, J. Kühn, T. Colomb, F. Monfort, E. Cuche, Y. Emery, K. Weible, P. Marquet, and C. Depeursinge, "Characterization of microlenses by digital holographic microscopy," Appl. Opt. **45**, 829–835 (2006).
32. B. E. Saleh and M. C. Teich, *Fundamentals of Photonics* (Wiley, 1991).
33. T. Colomb, F. Dürr, E. Cuche, P. Marquet, H. Limberger, R.-P. Salathé, and C. Depeursinge, "Polarization microscopy by use of digital holography: application to optical fiber birefringence measurements," Appl. Opt. **44**, 4461–4469 (2005).
34. F. Montfort, T. Colomb, F. Charrière, J. Kühn, P. Marquet, E. Cuche, S. Herminjard, and C. Depeursinge, "Submicrometer optical tomography by multiple wavelength digital holographic microscopy," Appl. Opt. (to be published).